# Epitaxial MoC<sub>x</sub>: competition between cubic $\delta$ -MoC<sub>y</sub>(111) and hexagonal $\beta$ -Mo<sub>2</sub>C(0001)

Peijiao Fang, Baiwei Wang, and Daniel Gall
Department of Materials Science and Engineering, Rensselaer Polytechnic Institute, Troy, NY
12180. USA

Molybdenum carbide thin films, 63-97 nm thick, are deposited by reactive DC magnetron sputtering onto Al<sub>2</sub>O<sub>3</sub>(0001) substrates at 1200 °C in 5 mTorr Ar - CH<sub>4</sub> gas mixtures with a varying CH<sub>4</sub> fraction  $f_{\text{CH4}} = 0$ -10%. X-ray diffraction  $\theta$ -2 $\theta$  scans,  $\omega$ -rocking curves,  $\phi$ -scans, and reciprocal space maps in combination with electron backscatter diffraction phase maps reveal that  $f_{\text{CH4}} = 7$ -8% leads to epitaxial  $\delta$ -MoC<sub>y</sub>(111) grains with  $[11\bar{2}]_{\delta\text{MoC}} \parallel [11\bar{2}0]_{\text{Al2O3}}$  and biaxial textured  $\beta$ -Mo<sub>2</sub>C(0001) with a preferential  $[10\bar{1}0]_{\beta\text{-Mo}2\text{C}} \parallel [10\bar{1}0]_{\text{Al2O3}}$  in-plane orientation. The two phases nucleate epitaxially on the substrate and/or on top of each other, followed by a competitive growth mode which results in a dominant cubic  $\delta$ -MoC<sub>y</sub>(111) or hexagonal  $\beta$ -Mo<sub>2</sub>C(0001) phase at  $f_{\text{CH4}} = 7$  or 8%, respectively, and a reduction in the layer density measured by x-ray reflectivity which suggests the formation of amorphous C clusters above the layer nucleation stage. Deposition at lower  $f_{\text{CH4}} \le 6\%$  leads to polycrystalline  $\beta$ -Mo<sub>2</sub>C and/or bcc Mo phases, while higher  $f_{\text{CH4}} \ge 10\%$  yields nanocrystalline  $\delta$ -MoC<sub>y</sub> embedded in an amorphous C matrix. The increase in  $f_{\text{CH4}}$  also causes a 3-fold decrease in the Mo deposition rate measured by Rutherford backscattering spectrometry and an 18% increase in the discharge voltage which is attributed to adsorbed CH<sub>4</sub> and carbide formation on the target surface.

Keywords: molybdenum carbide, epitaxy, x-ray diffraction, hard coating, sputter deposition, competitive growth

#### I. INTRODUCTION

Transition metal carbides exhibit a high hardness and electrical conductivity and are therefore promising for a wide range of technological applications including wear-resistant and decorative coatings [1-6], components for cutting and drilling tools [7, 8], electrical contacts [9, 10] and diffusion barriers [11] in microelectronics, and electrodes and catalysts for electrochemical storage and conversion systems [12-14]. Most of the early transition metals (groups 4-6) form interstitial carbides with cubic rocksalt, simple hexagonal or hexagonal close-packed structures, among which titanium and tungsten carbides are most extensively studied [15]. In contrast, molybdenum carbide is much less explored but has recently gained interest because Mo<sub>2</sub>C exhibits metallic conductivity and catalytic activity for the hydrogen evolution reaction and is therefore a promising material for noble-metal-free electrochemical energy conversion devices [16-18]. The hydrogen binding energy and the catalytic activity have been reported to be a strong function of the relative position of the d-band center and the Fermi level [19, 20] which, in turn, is controlled by the carbon-to-molybdenum ratio y and the exposed crystal surfaces [14]. The Mo<sub>2</sub>C activity is also enhanced by nanostructuring [21-25], conductive supports [26, 27], doping [28, 29] and surface/interface engineering [30-32]. Despite these reported efforts, relatively little is known about the fundamental intrinsic properties of  $MoC_{\nu}$  as a function of y, the phase, and the exposed surface. We envision that reactive sputter deposition and particularly the epitaxial growth of molybdenum carbide layers will facilitate studying its intrinsic properties by providing phase pure samples with a single surface orientation and without the confounding effects from grain boundaries. In addition, the epitaxial growth of molybdenum carbide is a model system to study the microstructural development of refractory transition metal carbide phases during thin film deposition. This approach of using epitaxy to both study the processes during thin film growth and provide samples for reliable physical property measurements has already been successfully employed for most of the early transition metal nitrides [33-46]. In contrast, only a few studies report on the epitaxial growth of transition metal carbides [47-53].

The four most common carbide phases in the Mo-C system are hexagonal β-Mo<sub>2</sub>C (ABAB), NaCl-structure  $\delta$ -MoC<sub> $\nu$ </sub> (ABCABC), hexagonal  $\eta$ -MoC<sub> $\nu$ </sub> (ABCACB) and WC-structure γ-MoC (AAAA) [54-56]. Here we use y to represent the C-to-Mo ratio in the carbide phase but note that some previous studies use "1-x" instead of y to indicate that molybdenum carbide is under-stoichiometric. These four phases all exhibit close-packed Mo planes which are stacked in different sequences as indicated by the letters A, B, and C. The carbon atoms occupy octahedral or trigonal-prismatic sites and form intercalated planes between the close-packed Mo planes and contain carbon vacancies except for the stoichiometric \( \gamma \) MoC phase. The homogeneity range for the  $\delta$ -MoC<sub>v</sub> and  $\eta$ -MoC<sub>v</sub> phases are v = 0.66-0.75 and 0.57-0.68, respectively [2]. Note that v < 1, indicating that C-vacancies are required to stabilize these phases [56]. In addition, stoichiometric  $\delta$ -MoC is not even metastable as it exhibits phonon instabilities [57]. The β-Mo<sub>2</sub>C contains 43-65% carbon vacancies corresponding to y = 0.35-0.57, and can be further subdivided into  $\beta''$ -Mo<sub>2</sub>C,  $\beta'$ -Mo<sub>2</sub>C and β-Mo<sub>2</sub>C depending on the ordering of carbon vacancies [56]. Reports on the thin film growth of molybdenum carbide on stainless steel, Si(001) and MgO(001) substrates indicate the formation of polycrystalline or nanocrystalline microstructures containing  $\delta$ -MoC<sub>y</sub>,  $\beta$ -Mo<sub>2</sub>C, a-C or other ternary carbides deposited by atom beam sputtering [58], magnetron sputtering [51, 59-63], atomic layer deposition [64], or pulsed-laser deposition [65]. In addition, a few studies report the epitaxial growth of cubic  $\delta$ -MoC<sub>v</sub> on MgO(001) and sapphire(0001) [51, 52, 65], and

molybdenum oxycarbide on MgO(110) [59], using evaporated C<sub>60</sub> [52] or CH<sub>4</sub> gas [51, 59, 65] as carbon source.

In this paper, we report on the growth competition between epitaxial cubic  $\delta$ -MoC<sub>y</sub> and hexagonal  $\beta$ -Mo<sub>2</sub>C during reactive DC magnetron sputter deposition on single crystal Al<sub>2</sub>O<sub>3</sub>(0001) substrates from a Mo target in 5 mTorr Ar/CH<sub>4</sub> gas mixtures at 1200 °C. The deposited microstructure is a strong function of the methane fraction  $f_{\text{CH4}} = 0$ -10% in the gas mixture, transitioning with increasing  $f_{\text{CH4}}$  from metallic Mo to mixed phases containing bcc Mo,  $\beta$ -Mo<sub>2</sub>C, and  $\delta$ -MoC<sub>y</sub>, and to nanocrystalline  $\delta$ -MoC<sub>y</sub> embedded in an amorphous carbon matrix. Structural analyses by x-ray diffraction and electron backscatter diffraction indicate a growth competition between epitaxial  $\delta$ -MoC<sub>y</sub>(111) which exhibits two 60°-rotated in-plane orientations, and bi-axial textured hexagonal Mo<sub>2</sub>C(0001).

## II. EXPERIMENTAL PROCEDURE

Molybdenum carbide layers were deposited in a three-chamber ultra-high vacuum DC magnetron sputtering system with a base pressure of  $10^{-9}$  Torr [40, 66]. Single-side polished  $10 \times$  $10 \times 0.5 \text{ mm}^3$  single-crystal Al<sub>2</sub>O<sub>3</sub>(0001) substrates were successively cleaned in ultrasonic baths of trichloroethylene, acetone, isopropyl alcohol, and deionized water for 20 min each. They were mounted onto a Mo holder using silver paint and inserted into the deposition system through a load-lock chamber. The substrates were degassed in vacuum for 1h at 1200 °C and kept at the same temperature for thin film deposition. 99.999% pure Ar which was further purified with a MicroTorr purifier and 99.999% pure CH<sub>4</sub> were introduced into the deposition chamber through needle valves to reach a constant total pressure of 5 mTorr, while varying the CH<sub>4</sub> fraction  $f_{\text{CH4}}$ from 0% to 10% to obtain a sample set with varying C content. We note that the high processing gas purity as well as the base pressure of the deposition system results in an expected negligible oxygen impurity concentration in the deposited layers. The target was a 5-cm-diameter 0.6-cmthick 99.95% Mo disk positioned 9 cm from the substrate at a 45° tilt. It was sputter etched for 10 min prior to each deposition with a shutter shielding the substrate. The sample stage was rotated at 60 rpm to ensure uniform deposition. A constant DC power of 50 W was applied to the molybdenum target, yielding a Mo deposition rate that decreases with increasing  $f_{CH4}$  from  $62\times10^{15}$ to 23×10<sup>15</sup> Mo atoms·cm<sup>-2</sup>·min<sup>-1</sup>, resulting in a film thickness range of 63-97 nm for a constant deposition time of 10 min.

X-ray diffraction measurements were performed with a Panalytical X'pert PRO MPD system with a Cu source using a 45 kV accelerating volage and a 40 mA current. Sample and beam alignment included direct beam alignment, sample height adjustment, as well as correction of the substrate  $\omega$  and  $\chi$  tilt angles. Symmetric  $\theta$ -2 $\theta$  scans were obtained using a parallel beam geometry with an X-ray mirror (divergence < 0.055°) in combination with a PIXcel solid-state line detector operated in receiving mode with a 0.165 mm active length, which effectively acts as a point detector. Both CuK $_{\alpha 1}$  and CuK $_{\alpha 2}$  radiation with wavelengths  $\lambda$  = 1.5406 and 1.5444 Å pass through the X-ray mirror, yielding an average weighted  $\lambda$  = 1.5419 Å.  $\omega$  rocking curves were obtained with the same parallel beam geometry at a constant 2 $\theta$  angle corresponding to the  $\delta$ -MoC $_y$  111 or  $\beta$ -Mo $_2$ C 0002 reflections.  $\phi$ -scans were acquired with constant  $\chi$  tilts and 2 $\theta$  angles to detect  $\delta$ -MoC $_y$  113,  $\beta$ -Mo $_2$ C 10 $\overline{1}$ 3 and Al $_2$ O $_3$  1 $\overline{1}$ 04 reflections, using a point source in combination with an x-ray lens yielding a quasi-parallel beam with an equatorial and axial divergence of 0.3°. Asymmetric

reciprocal space maps were acquired around  $\delta$ -MoC<sub>y</sub> 113,  $\beta$ -Mo<sub>2</sub>C 10 $\overline{1}$ 3 and Al<sub>2</sub>O<sub>3</sub> 11 $\overline{2}$ 9 reflections using the X-ray mirror and taking advantage of all 256 channels of the solid state line detector. This was done with a small diffracted beam exit angle ~10° with respect to the sample surface to cause beam narrowing which increases the 2 $\theta$  resolution. In addition, symmetric  $\theta$ -2 $\theta$  scans with a Bragg-Brentano divergent beam geometry were collected over a large 2 $\theta$  = 5-85° range in order to detect small inclusions of possible secondary phases or misoriented grains. X-ray reflectivity (XRR) scans were obtained with the same diffractometer and data fitting was accomplished using the X'pert Reflectivity simulation program based on the Parratt formalism for reflectivity [67].

Rutherford Backscattering Spectrometry (RBS) was conducted using a 2.00 MeV <sup>4</sup>He<sup>+</sup> ion beam incident at an angle of 6° relative to the sample surface normal, and a total scattering angle of 166° between the incident beam and the detector. The Mo atomic areal densities were determined from RBS spectra using the SIMNRA simulation software [68]. Electron backscatter diffraction (EBSD) micrographs were acquired in a Carl Zeiss 1540EsB Crossbeam scanning electron microscope with a 15 kV accelerating voltage, a 60 µm aperture for high current mode, an 18 mm working distance and an OXFORD INSTRUMENTS NordlysNano EBSD detector.

## III. RESULTS AND DISCUSSION

Figure 1(a) shows typical x-ray reflectivity plots from  $MoC_x$  layers deposited with  $f_{CH4} =$ 6, 7 and 8%. The measured intensity (solid lines) is plotted in a logarithmic scale over  $2\theta = 0.5$ -2.5° and the results from data fitting are shown as dotted lines which are shifted for clarity purposes by a factor of 3. The pattern from the MoC<sub>x</sub> film with  $f_{CH4} = 6\%$  shows a critical angle of 0.76°, an overall decrease in the measured intensity with increasing  $2\theta$ , and interference fringes associated with reflections from the MoC<sub>x</sub> surface and the MoC<sub>x</sub>-Al<sub>2</sub>O<sub>3</sub>(0001) interface. The dotted line from data fitting describes the measured intensity well and yields a layer density of  $9.2 \pm 0.1$  g/cm<sup>3</sup>, a thickness of  $70.3 \pm 0.3$  nm and a surface roughness of  $1.3 \pm 0.3$  nm. The measured density is in excellent agreement with the reported 9.18 g/cm<sup>3</sup> for Mo<sub>2</sub>C [69, 70], which is the primary phase for this layer as discussed below. The plotted curve for  $f_{\text{CH4}} = 7\%$  decreases above a critical angle of 0.70°, which is 8% smaller than for  $f_{CH4} = 6\%$  and suggests a reduced density. The measured intensity shows no net decrease between  $2\theta = 0.8$  and  $1.1^{\circ}$  and only a few interference fringes can be detected, indicating a non-uniform density and considerable surface or interface roughness. Consequently, the pattern cannot be explained by a single homogeneous film and data fitting is done using a two-layer model where the film is composed of a thin and dense interface layer near the substrate and a lower-density top layer. Data fitting yields a 7-nm-thick interface layer and a 73-nm-thick bulk layer, with densities of 8.4 and 7.3 g/cm<sup>3</sup>, and a roughness of 2.0 nm between the two layers and a 4.8 nm roughness of the top surface. The density of the interface layer is close to reported values for cubic  $\delta$ -MoC<sub>v</sub> of 8.81, 8.13 and 8.56 g/cm<sup>3</sup> from both experimental and computational studies [71-73]. The density in the bulk of the layer is 13% below that of the interface-layer and suggests the presence of segregated clusters of low-density graphitic or amorphous carbon, as discussed below. The pattern for  $f_{CH4} = 8\%$  exhibits only two detectable fringe minima and a critical angle of  $0.65^{\circ}$  which is even lower than for  $f_{\text{CH4}} = 7\%$ . Data fitting using a two-layer structure yields an 18-nm interface layer with a density of 8.5 g/cm<sup>3</sup> and a roughness of 4.5 nm, and a 45-nm bulk layer with a density of 6.8 g/cm<sup>3</sup> and a roughness of 8 nm.

Figure 1(b) is a plot of the Mo target (cathode) voltage  $V_t$  and of the Mo deposition rate R vs the methane fraction during carbide layer deposition.  $V_t$  increases nearly linearly from 327 V for deposition of pure bcc Mo ( $f_{\text{CH4}} = 0\%$ ) to 386 V for Mo carbide deposition with  $f_{\text{CH4}} = 10\%$ .

The corresponding cathode current decreases from 0.12 to 0.10 A, because the power supply is operated in a constant power mode. The increasing voltage with increasing  $f_{CH4}$  is attributed to a decrease in the secondary electron yield as the target surface becomes increasingly covered with CH<sub>x</sub> fragments, MoC<sub>x</sub>, and/or graphitic C. This effect is typically referred to as target poisoning and is common for reactive sputter deposition of nitrides and carbides from metal targets [74, 75]. The Mo deposition rate is plotted in Fig. 1(b) in units of Mo atoms per area and time. The square symbols are the results from XRR analyses, while the diamonds indicate the corresponding values determined by RBS measurements for the layers with  $f_{CH4} = 6\%$ , 7%, and 8%. R decreases from  $(62.0 \pm 0.5) \times 10^{15}$  atoms·cm<sup>-2</sup>·min<sup>-1</sup> for  $f_{CH4} = 0\%$  to  $(45 \pm 4)$ ,  $(38.0 \pm 0.2)$ ,  $(31 \pm 3)$  and  $(23 \pm 2)$  $\times$  10<sup>15</sup> atoms·cm<sup>-2</sup>·min<sup>-1</sup> for  $f_{CH4} = 4\%$ , 6%, 7%, and 8%, respectively, as determined from the thickness and density measured by XRR and assuming dense microstructures and Mo,  $\beta$ -Mo<sub>2</sub>C,  $\delta$ -MoC<sub>v</sub>, and a-C phases with their corresponding atomic densities. Independent determination of the Mo areal density from RBS spectra for  $f_{\text{CH4}} = 6\%$ , 7%, and 8% yields  $R = (37 \pm 0.5)$ ,  $(32.5 \pm 0.5)$ , and  $(25.5 \pm 0.5) \times 10^{15}$  atoms·cm<sup>-2</sup>·min<sup>-1</sup>, respectively, in excellent agreement with the XRR results. The decrease in the Mo deposition rate is attributed to an increase in the cohesive energy per Mo atom of the compound layer that forms on the target surface with increasing  $f_{\rm CH4}$  [76]. That is, target poisoning causes not only an increase in  $V_t$  but also an even more pronounced reduction in the Mo sputtering rate.

Figure 2 is a plot of the carbon-to-molybdenum ratio x in the MoC<sub>x</sub> layers vs the methane fraction  $f_{CH4} = 0$  to 8% during deposition. We note that the plotted x refers to the total C-to-Mo ratio within the layers which includes a possible segregated carbon phase, while we use the subscript y to denote the C-to-Mo ratio in specific  $MoC_v$  phases. The measured composition is determined by XRR and RBS using two methods for carbon poor and carbon rich samples as indicated by purple squares and green triangles, respectively. Each data point is labeled with the relevant phases determined from the XRD analyses presented below. The layers deposited with  $f_{\text{CH4}} = 0$ , 4 and 6% are "carbon poor", with x = 0, 0.38 ± 0.13, and 0.56 ± 0.09, respectively. These x values are determined from the layer thickness and mass density  $\rho$  (in g/cm<sup>3</sup>) measured by XRR and the lattice constants from the XRD analyses discussed below, assuming no Mo vacancies in  $\beta$ -Mo<sub>2</sub>C and  $\delta$ -MoC<sub> $\nu$ </sub>. The latter assumption is based on the reported instability of cation vacancies in cubic molybdenum carbide [77] and the related TiC [78]. For example, the  $f_{\rm CH4} = 6\%$  layer has a measured  $\rho = 9.2 \text{ g/cm}^3$  and consists of phase-pure  $\beta$ -Mo<sub>2</sub>C with an atomic density of  $5.4 \times 10^{22}$ Mo atoms/cm<sup>3</sup> which corresponds to 8.6 g/cm<sup>3</sup>. The density difference of 0.6 g/cm<sup>3</sup> is from interstitial carbon and corresponds to  $3.0 \times 10^{22}$  C atoms/cm<sup>3</sup>, yielding the plotted x = 0.56. The layer with  $f_{\text{CH4}} = 4\%$  has a measured  $\rho = 9.3 \text{ g/cm}^3$  and consists of both bcc Mo and  $\beta$ -Mo<sub>2</sub>C phases. The density of bcc Mo is 10.2 g/cm<sup>3</sup> and the density of stoichiometric  $\beta$ -Mo<sub>2</sub>C is 9.1 g/cm<sup>3</sup>. Thus, the measured average  $\rho = 9.3$  g/cm<sup>3</sup> suggests an 82:18 mixture of bcc Mo and  $\beta$ -Mo<sub>2</sub>C, yielding  $2.1 \times 10^{22}$  C atoms/cm<sup>3</sup> and x = 0.38. However, considering the possible C-to-Mo range of 0.35-0.57 in  $\beta$ -Mo<sub>2</sub>C [56] results in a corresponding  $\rho = 8.97-9.21$  g/cm<sup>3</sup> of the carbide and x = 0.25-0.51 of the two phase mixture. Thus, we conclude  $x = 0.38 \pm 0.13$  for  $f_{\text{CH4}} = 4\%$ .

The green triangle data points in Fig. 2 for the C-rich samples are obtained using data from both RBS and XRR measurements. More specifically, the molybdenum areal density  $\Theta_{Mo}$  (in atoms/cm<sup>2</sup>) is directly measured by RBS. In contrast, RBS is not well suited to directly measure the carbon areal density  $\Theta_{C}$  due to the small back-scattering cross-section for carbon atoms which would yield a large experimental uncertainty in  $\Theta_{C}$ . Instead, we deduce  $\Theta_{C}$  using  $\Theta_{Mo}$  and the total density and layer thickness from XRR. For example, the  $f_{CH4} = 6\%$  film has a measured  $\Theta_{Mo} = 3.7$ 

 $\times$  10<sup>17</sup> cm<sup>-2</sup> which corresponds to a Mo density for this 70.3-nm-thick layer of 8.4 g/cm<sup>3</sup>. Comparing this density to  $\rho = 9.2$  g/cm<sup>3</sup> measured by XRR suggests that 0.8 g/cm<sup>3</sup> should be attributed to C, yielding  $x = 0.76 \pm 0.08$ , in reasonable agreement with  $0.56 \pm 0.09$  determined with XRR alone. The same analyses for the  $f_{\text{CH4}} = 7$  and 8% layers yields  $x = 1.1 \pm 0.4$  and  $1.0 \pm 0.4$ , respectively. We note that this analysis excludes the contribution from possible hydrogen, which could incorporate from the CH<sub>4</sub> gas into the amorphous carbon phase for layers with large x, but has a negligible impact (< 1%) on the total mass and is therefore neglected.

Figure 3 shows sections of typical X-ray diffraction  $\theta$ -2 $\theta$  and  $\omega$  rocking curve scans from MoC<sub>x</sub> layers deposited with  $f_{CH4} = 4-10\%$ . The  $\theta$ -2 $\theta$  pattern in Fig. 3(a) from a  $f_{CH4} = 10\%$  layer was obtained using a powder scan with a divergent beam to maximize intensities from randomly oriented polycrystalline or nanocrystalline grains and is plotted in a linear scale over  $2\theta = 36 - 43^{\circ}$ . In contrast, the patterns in Fig. 3(b) for  $f_{CH4} = 4 - 8\%$  were acquired with a parallel beam geometry to enhance the diffracted intensities from highly oriented films and are plotted in a logarithmic scale with patterns offset by 0, 3, 6 and 9 orders of magnitude for clarity purposes. The pattern from the layer grown with  $f_{\text{CH4}} = 4\%$  exhibits a double peak feature at  $2\theta = 41.685^{\circ}$  and  $41.793^{\circ}$ from the substrate Al<sub>2</sub>O<sub>3</sub> 0006 diffraction of the CuK $\alpha_1$  and CuK $\alpha_2$  radiation. It also shows peaks at  $2\theta = 40.53$ , 37.93, and 39.40° attributed to the 110 reflection of bcc Mo and the 0002 and  $10\overline{1}1$ reflections of the hexagonal  $\beta$ -Mo<sub>2</sub>C phase, respectively, as labeled with diamond and triangle symbols in Fig. 3(b). These three peaks have  $\omega$  rocking curve (not shown) full-widths at halfmaximum  $\Gamma_{\omega} = 0.26$ , 0.26 and 0.24°, respectively, indicating very strong out-of-plane alignment which suggests local epitaxial growth of bcc Mo as well as  $\beta$ -Mo<sub>2</sub>C with both 0002 and  $10\overline{1}1$ orientation. The pattern from the  $f_{\text{CH4}} = 6\%$  layer shows the same substrate double-peak as well as 0002 and  $10\overline{1}1$  peaks from  $\beta$ -Mo<sub>2</sub>C at  $2\theta = 37.93$  and  $39.44^{\circ}$ , but no detectable peak from bcc Mo. This indicates that  $f_{CH4} = 6\%$  is sufficient for complete carburization. The rocking curve widths of the  $\beta$ -Mo<sub>2</sub>C 0002 and 1011 peaks are 0.29° and 0.35°, respectively, indicating comparable excellent crystalline alignment as for the  $f_{CH4} = 4\%$  layer. The XRD peak positions for both 4% and 6% layers are in good agreement with the reported Mo 110 reflection at 40.416° (JCPDS 001-1205) and the  $\beta$ -Mo<sub>2</sub>C 0002 and 10 $\overline{1}$ 1 reflections at 38.101° and 39.492° (JCPDS 001-1188). Increasing  $f_{\text{CH4}}$  further to 7% leads to a molybdenum carbide layer that exhibits only a single peak in the  $\theta$ -2 $\theta$  scan. It is attributed to the 111 reflection of cubic  $\delta$ -MoC<sub>v</sub> and is at 2 $\theta$ = 36.71°, which is in reasonable agreement with the reported  $2\theta$  values of 36.388° (JCPDS 073-9798), 37.08° [65] and 37.768° (JCPDS 015-0457). We note that this peak could also be attributed to an  $\eta$ -MoC<sub> $\nu$ </sub> 0006 reflection with an expected  $2\theta = 36.774^{\circ}$  (JCPDS 008-0384). However, based on the  $\phi$ -scan and reciprocal space map analyses presented below, the peak for  $f_{\rm CH4} = 7\%$  is clearly due to  $\delta$ - $MoC_v$ . This  $\delta$ - $MoC_v$  111 peak also has a broad tail on the right side that extends to approximately  $2\theta = 38^{\circ}$ , suggesting that this layer may contain some  $\beta$ -Mo<sub>2</sub>C which has an expected  $2\theta = 38.101^{\circ}$ (JCPDS 001-1188) for the 0002 reflection. The rocking curve for this 111 peak is shown in Fig. 3(c). It has a relatively wide width  $\Gamma_{\omega} = 2.4^{\circ}$  which is determined by Gaussian fitting and is attributed to an increased mosaicity (mosaic spread) caused by relaxation of the  $\delta$ -MoC<sub> $\nu$ </sub> film and the related dislocation formation, as discussed below in connection with the reciprocal space map analysis. We note that this rocking curve also includes a small sharp peak at the center top of the curve, which has a width of  $0.1^{\circ}$  and is attributed to the  $\beta$ -Mo<sub>2</sub>C minority phase. We note that the width of the tail at  $2\theta = 38^{\circ}$  also has a narrow 0.1° rocking curve (not shown), confirming the high crystalline alignment of the minority  $\beta$ -Mo<sub>2</sub>C. The pattern from the film deposited with  $f_{CH4} = 8\%$ shows a  $\beta$ -Mo<sub>2</sub>C 0002 peak at  $2\theta = 37.89^{\circ}$  and a shoulder at 37.28° which is approximately one

order of magnitude less intense and is associated with the cubic  $\delta$ -MoC<sub>y</sub> 111 reflection, as discussed below. The 0002 peak has a narrow rocking curve with  $\Gamma_{\omega} = 0.1^{\circ}$  as shown in Fig. 3(d), indicating excellent crystalline alignment of  $\beta$ -Mo<sub>2</sub>C and suggesting epitaxial growth as confirmed by reciprocal space mapping presented below. In addition, the rocking curve also includes a weaker and broader peak with  $\Gamma_{\omega} = 0.5^{\circ}$ , as determined from Gaussian fitting. It is attributed to a relaxed cubic minority phase, consistent with the reciprocal space map analyses below. The pattern from the  $f_{\text{CH4}} = 10\%$  layer shown in Fig. 3(a) is obtained using a divergent x-ray source because no peak could be detected with the parallel beam setup employed for  $f_{\text{CH4}} = 4$ -8%. It shows a weak 111  $\delta$ -MoC<sub>y</sub> peak, indicating a polycrystalline microstructure with low crystalline quality which is attributed to excess carbon that segregates to form amorphous or graphitic carbon and causes continuous carbide renucleation during deposition and a resulting nanocrystalline structure. Similar powder scans with a divergent beam were performed for all films to detect small concentrations of impurity phases or misoriented grains. However, no additional XRD reflections could be detected over the entire  $2\theta = 5$  - 85° range, with the exception of higher-order reflections of peaks already discussed and shown in Fig. 3(b).

Figures 4(a-c) are x-ray diffraction  $\phi$ -scans showing asymmetric Al<sub>2</sub>O<sub>3</sub>  $1\overline{1}$ 04,  $\delta$ -MoC<sub> $\nu$ </sub> 113, and  $\beta$ -Mo<sub>2</sub>C 1013 reflections from a substrate and from layers deposited with  $f_{CH4} = 7$  and 8%, respectively. The pattern in Fig. 4(a) is obtained by fixing  $2\theta = 35.137^{\circ}$  and tilting the sample about the surface normal by  $\chi = 38.3^{\circ}$  to detect Al<sub>2</sub>O<sub>3</sub> 1 $\overline{1}$ 04 reflections. It has three peaks at  $\phi =$ 90.9°, 210.2° and 329.9° which confirm the 3-fold orientation symmetry of the substrate. This measurement is done for all samples for which  $\phi$ -scans are acquired and is used to accurately determine the in-plane orientation of the substrate. The pattern in Fig. 4(b) is obtained from the layer with  $f_{CH4} = 7\%$  and uses  $2\theta = 73.438^{\circ}$  and  $\chi = 29.5^{\circ}$  to detect  $\delta$ -MoC<sub> $\nu$ </sub> 113 reflections. It shows peaks at  $\phi = 60.8^{\circ}$ , 121.0°, 180.9°, 241.1°, 300.9°, and 360.8°, indicating a 6-fold rotational symmetry which is confirmed by the EBSD  $\delta$ -MoC<sub> $\nu$ </sub> {111} pole figure shown in the inset of Fig. 4(d). We note that 113 reflections for cubic crystals have only a 3-fold symmetry about the [111] direction, indicating that the  $f_{\text{CH4}} = 7\%$  layer contains two  $\delta$ -MoC<sub> $\nu$ </sub> domains which have a common [111] axis perpendicular to the Al<sub>2</sub>O<sub>3</sub>(0001) substrate surface and are 60° rotated with respect to each other. Comparing the peak positions for Al<sub>2</sub>O<sub>3</sub>  $1\overline{1}$ 04 and  $\delta$ -MoC<sub>y</sub> 113 in Figs. 4(a) and (b) indicates a 30° in-plane rotation, indicating an in-plane epitaxial relationship with  $[11\overline{2}]_{\mathcal{E}_{MOC}}$  $[11\overline{2}0]_{Al2O3}$  or  $[11\overline{2}]_{\mathcal{E}MoC} \parallel [2\overline{1}\overline{1}0]_{Al2O3}$ . The pattern in Fig. 4(c) is from the layer deposited with  $f_{\rm CH4} = 8\%$ . It is obtained with  $2\theta = 69.583^{\circ}$  and  $\chi = 31.2^{\circ}$  to detect asymmetric  $\beta$ -Mo<sub>2</sub>C  $10\overline{1}3$ reflections. We note that these values are close to those for the  $\delta$ -MoC<sub> $\nu$ </sub> 113 reflections such that weak intensities from  $\delta$ -MoC<sub>y</sub> may also be detected. This  $\phi$ -scan exhibits a 6-fold symmetry with a set of peaks at 60°, 120°, 180°, 240°, 300° and 360° and a set of triplets with their strongest central peaks at 30°, 90°, 150°, 210°, 270° and 330°, two slightly weaker peaks at  $\pm$  10° from the central peaks, and plateaus at  $\pm 25^{\circ}$  about the central peaks with an intensity of 30-50% of the peak intensity. The first set of peaks is located at the same  $\phi$  values as the  $\delta$ -MoC<sub> $\nu$ </sub> 113 reflections shown in Fig. 4(b) and is attributed to a minority cubic  $\delta$ -MoC<sub> $\nu$ </sub> phase which forms during the initial stages of film growth in this  $f_{CH4} = 8\%$  layer, which is confirmed from a thinner sample deposited at the same condition as discussed below. The triplets as well as the plateaus are attributed to  $\beta$ -Mo<sub>2</sub>C  $10\overline{1}3$  reflections and suggest an in-plane epitaxial relationship with  $[10\overline{1}0]_{\beta \text{Mo}2\text{C}} \parallel [10\overline{1}0]_{\text{Al}2\text{O}3}$  for the central peaks, a preferred 10° rotation from this epitaxial orientation about the  $\beta$ -Mo<sub>2</sub>C 0001 axis, or an arbitrary rotation by any angle between -25° and +25° from this epitaxial relationship. We attribute the diverse in-plane orientations to the 9.5% lattice misfit between the basal planes of  $\beta$ -Mo<sub>2</sub>C and Al<sub>2</sub>O<sub>3</sub>.

Figure 4(d) is an EBSD phase map of the molybdenum carbide layer deposited at  $f_{\text{CH4}} = 7\%$ . It shows the cubic δ-MoC<sub>y</sub> phase in blue, the hexagonal β-Mo<sub>2</sub>C phase in red, and pixels for which the Kikuchi patterns cannot be unambiguously assigned in black. The majority of the micrograph is blue, consistent with the XRD results indicating that this layer contains primarily cubic δ-MoC<sub>y</sub>. Approximately 17% of the micrograph is red, suggesting that a corresponding fraction of the layer has crystalized in the β-Mo<sub>2</sub>C phase. These β-Mo<sub>2</sub>C grains have a width of 10-50 nm. We attribute the black areas to pixels with phase boundaries, possible misoriented grains, and/or surface-segregated carbon which blurs the collected Kikuchi pattern. The inset is an EBSD 111 pole figure from the cubic δ-MoC<sub>y</sub> phase, showing an intense central spot and 6-fold symmetric peaks at  $\chi = 71^{\circ}$ . This indicates two domains with a 111 out-of-plane orientation which are 60° rotated with respect to each other, confirming the XRD results in Figs. 3(b), 3(c), and 4(b). Similar two-domain structures are common for 111-oriented fcc metals deposited on Al<sub>2</sub>O<sub>3</sub>(0001) [79, 80].

Figures 5(a) and (b) show asymmetric x-ray diffraction reciprocal space maps from layers deposited at  $f_{CH4} = 7$  and 8%, respectively. The blue-to-red or pink-to-red colors indicate the measured intensity in a logarithmic scale from 35 to 10<sup>6</sup> counts, plotted in reciprocal space where the in-plane and out-of-plane reciprocal lattice vectors  $k_{\parallel}$  and  $k_{\perp}$  are related to the experimental  $\omega$ and  $\theta$  according to  $k_{\parallel} = 2\sin\theta\sin(\omega\theta)/\lambda$  and  $k_{\perp} = 2\sin\theta\cos(\omega\theta)/\lambda$ , where  $\lambda = 1.5419$  Å is the weighted average from the  $CuK\alpha_1$  and  $CuK\alpha_2$  lines. The arrows in Fig. 5(b) indicate the experimental  $\omega$  and  $\omega$ -2 $\theta$  directions, which are rotated by 31° with respect to the axes of the plot, corresponding to the angle between  $Al_2O_3$  (0001) and (11 $\overline{2}$ 9) planes. Fig. 5(a) contains the data from two maps around the  $Al_2O_3$   $11\overline{2}9$  and the  $\delta$ -MoC<sub>y</sub> 113 reflections, where the blue parallelogram borders indicate the limits of the measured  $\omega$  and  $2\theta$  ranges. Both maps are labeled with  $\phi = 0^{\circ}$ , defining the azimuthal rotation which, consistent with Fig. 4(a), indicates that  $k_{\parallel}$  is along the direction of Al<sub>2</sub>O<sub>3</sub>[11<del>2</del>0]. The substrate 11<del>2</del>9 reflection shows a double-peak feature due to the CuK  $\alpha_1$  and CuK  $\alpha_2$  x-ray lines, with the weighted average at  $k_{\parallel} = 4.203$  nm<sup>-1</sup> and  $k_{\perp} = 6.928$ nm<sup>-1</sup>. The substrate peaks show elongations along  $2\theta$ , along  $\omega$ -2 $\theta$ , and along  $\omega$  directions, which are attributed to resolution streaks from electronic noise in the line detector, to wavelength spreading of the x-ray source, and from mosaicity, respectively. The center of the MoC<sub>y</sub> 113 reflection in Fig. 5(a) is at  $k_{\parallel} = 3.84$  nm<sup>-1</sup> and  $k_{\perp} = 6.80$  nm<sup>-1</sup> which yields in-plane and perpendicular lattice constants  $a_{\parallel} = 0.425 \pm 0.001$  nm and  $a_{\perp} = 0.4246 \pm 0.0003$  nm, in agreement with  $a_{\perp} = 0.424$  nm measured with the symmetric XRD  $\theta$ -2 $\theta$  scan shown in Fig. 3(b). These values indicate a small in-plane tensile strain of 0.1% and a relaxed  $\delta$ -MoC<sub>v</sub> lattice constant of 0.425 nm determined using the previously reported Poisson's ratio of 0.29 [81]. The  $\delta$ -MoC<sub>y</sub> 113 peak has an elliptical shape with an elongation along the  $\omega$  direction which is attributed to mosaicity, while the broadening along the  $\omega$ -2 $\theta$  direction may be attributed to the finite layer thickness, strain fluctuations, and/or crystalline defects that limit the vertical coherence length. The peak width along  $\omega$  is  $\Gamma_{\omega} = 1.5^{\circ}$ , corresponding to an in-plane x-ray coherence length of 8 nm, in good agreement with 6 nm determined from  $\Gamma_{\omega} = 2.4^{\circ}$  of the symmetric  $\omega$  rocking curve shown in Fig. 3(c) from the same sample.

The map in Fig. 5(b) from the layer deposited with  $f_{\text{CH4}} = 8\%$  shows the double peak feature from the substrate Al<sub>2</sub>O<sub>3</sub> 11 $\overline{2}$ 9 reflection as well as a peak due to the  $\delta$ -MoC<sub>y</sub> 113 reflection located at  $k_{\parallel} = 3.83 \text{ nm}^{-1}$  and  $k_{\perp} = 6.82 \text{ nm}^{-1}$ . However, this latter peak is over an order of magnitude weaker

than the corresponding peak for  $f_{\text{CH4}} = 7\%$  film, confirming the result from the symmetric  $\theta$ -2 $\theta$ pattern in Fig. 3(b) that indicates that cubic  $\delta$ -MoC<sub> $\nu$ </sub> is a minority phase for  $f_{CH4} = 8\%$ . The map in Fig. 5(b) also shows a strong peak at  $k_{\parallel} = 3.840 \text{ nm}^{-1}$  and  $k_{\perp} = 6.335 \text{ nm}^{-1}$  which is attributed to the B-Mo<sub>2</sub>C 1013 reflection. It is plotted with a different (pink) color scheme because it is obtained using an azimuthal angle  $\phi = 30^{\circ}$  such that  $k_{\parallel}$  is along the Al<sub>2</sub>O<sub>3</sub> [10 $\overline{1}$ 0] direction. This peak is the same  $\beta$ -Mo<sub>2</sub>C 10 $\overline{1}$ 3 reflection shown in Fig. 4(c) at  $\phi = 30^{\circ}$ . The measured  $k_{\perp}$  yields an out-ofplane lattice constant  $c = 3 / k_{\perp} = 0.4736$  nm which is in good agreement (within 0.3%) with c =0.4749 nm obtained from the symmetric XRD  $\theta$ -2 $\theta$  scan in Fig. 3(b). The measured  $k_{\parallel}$  provides a value for the in-plane lattice constant  $a = b = 2 / (\sqrt{3} \times k_{\parallel}) = 0.3007$  nm which corresponds to the Mo-Mo distance within the close-packed plane of  $\beta$ -Mo<sub>2</sub>C(0001). This can be directly compared to the Mo-Mo distance in the close-packed 111-plane of  $\delta$ -MoC<sub> $\nu$ </sub>(111), which is  $a_{\parallel}/\sqrt{2} = 0.301 \pm 0.000$ 0.001 nm. These two values match (within 0.1%), suggesting that the two phases,  $\beta$ -Mo<sub>2</sub>C(0001) and  $\delta$ -MoC<sub>v</sub>(111), can grow epitaxially on top of each other without causing any considerable strain. This contributes to the complex growth competition between these two phases for  $f_{CH4} = 7\%$ and 8%, as discussed below. We note that this pink peak cannot be attributed to the 113 reflections from the  $\delta$ -MoC<sub>v</sub> minority phase because this would indicate a cubic lattice constant of 0.4559 nm, in clear disagreement (11% larger) with the 0.4110 nm obtained from the  $\theta$ -2 $\theta$  scan in Fig. 3(b).

Therefore, the reciprocal space maps in Fig. 5(b) confirm that the  $f_{CH4} = 8\%$  film contains both  $\beta$ -Mo<sub>2</sub>C and  $\delta$ -MoC<sub> $\nu$ </sub> phases. The two phases cause peaks with  $\Gamma_{\omega} = 0.1^{\circ}$  and  $0.4^{\circ}$  respectively, consistent with the two rocking curve widths of 0.1° and 0.5° in Fig. 3(d). These results suggest that both phases exhibit some degree of epitaxy and form during a competitive growth mode. Similarly, the two co-existing phases are also observed for the  $f_{CH4} = 7\%$  layer in the EBSD phase map in Fig. 4(d). We note that the  $\beta$ -Mo<sub>2</sub>C minority phase in the  $f_{CH4} = 7\%$  film cannot be detected in the  $\phi$ -scan and reciprocal space map, likely because of an insufficient  $10\overline{1}3$  reflection intensity. However, the asymmetric tail towards higher  $2\theta$  values in Fig. 3(b) and the rocking curve in Fig. 3(c) with a shape suggesting two distinct widths provide evidence for the two-phases. That is, the  $f_{\text{CH4}} = 7\%$  layer exhibits a similar competitive growth mode as the  $f_{\text{CH4}} = 8\%$  layer. To explore the phase competition further, thinner samples with a five times smaller deposition time were deposited for  $f_{\text{CH4}} = 7\%$  and 8%. They both show a  $\theta$ -2 $\theta$  diffraction peak at 36.8° with a wide asymmetric shoulder extending up to 38° (not shown), indicating predominantly  $\delta$ -MoC<sub>y</sub> with a β-Mo<sub>2</sub>C minority phase in the initial stages of growth. These thin (approximately 10 nm thick) layers exhibit  $\phi$ -scans similar to that shown in Fig. 4(b) and  $\delta$ -MoC<sub>v</sub> 111 rocking curves that are a sum of a narrow (0.1°) and a wide (2.3°) curve similar to that in Fig. 3(c) but with a 5-10 times larger fraction of the narrow vs the broad peak.

These overall results suggest that deposition with  $f_{\text{CH4}} = 7-8\%$  leads to (i) nucleation of  $\delta$ -MoC<sub>y</sub>(111) grains which are well aligned ( $\Gamma_{\omega} = 0.1^{\circ}$ ) with the Al<sub>2</sub>O<sub>3</sub>(0001) substrate, (ii)  $\beta$ -Mo<sub>2</sub>C(0001) grains which develop in the early stages of film growth either by direct nucleation on the substrate or epitaxial growth on the  $\delta$ -MoC<sub>y</sub>(111) nuclei, and (iii) MoC<sub>y</sub>(111) grains with a larger orientation variation ( $\Gamma_{\omega} = 2.5^{\circ}$ ) which form either by tilted nucleation on the substrate or by defect-containing epitaxial growth on well-aligned  $\delta$ -MoC<sub>y</sub>(111) nuclei. Subsequent layer growth leads to the competition between the  $\beta$ -Mo<sub>2</sub>C or  $\delta$ -MoC<sub>y</sub> grains, such that one of the two phases emerge during a competitive growth mode and dominate the microstructure for thicker layers. Both phases exhibit an epitaxial relationship with the Al<sub>2</sub>O<sub>3</sub>(0001) substrate and may even continue to grow epitaxially on top of each other. The final microstructure contains  $\delta$ -MoC<sub>y</sub>(111)

grains with a relatively broad  $\Gamma_{\omega} = 2.4^{\circ}$  but a well-defined in-plane alignment with two 60°-rotated domains, and  $\beta$ -Mo<sub>2</sub>C(0001) grains with a strong alignment in the growth direction with  $\Gamma_{\omega} = 0.1^{\circ}$ but a large  $\pm 25^{\circ}$  variation in the in-plane orientation. We note that it is not clearly understood which parameters control the growth competition between these two phases.  $f_{CH4} = 7\%$  leads to predominantly  $\delta$ -MoC<sub>v</sub> while increasing the CH<sub>4</sub> flux to  $f_{CH4} = 8\%$  results in a dominance of  $\beta$ -Mo<sub>2</sub>C. This is surprising because previous studies report larger C-to-Mo ratios for cubic  $\delta$ -MoC<sub> $\nu$ </sub> than hexagonal  $\beta$ -Mo<sub>2</sub>C [2, 56] and our own results indicate  $\beta$ -Mo<sub>2</sub>C for  $f_{CH4} \le 6\%$  and  $\delta$ -MoC<sub>v</sub> for  $f_{CH4} > 10\%$ . In addition, the layers which exhibit a mixture of the two phases in the nucleation stage ( $f_{CH4} = 7$  and 8%) also show a higher density near the bottom 7 and 18 nm, respectively, followed by growth of a lower-density structure which we attribute to excess C in the form of graphitic or amorphous C clusters. Thus, it is plausible that C surface segregation and CH<sub>4</sub> adsorption after the nucleation stage facilitates the transition to a single preferred phase during a  $\delta$ -MoC<sub>v</sub>(111) vs  $\beta$ -Mo<sub>2</sub>C(0001) competitive growth mode. In that case, the larger expected CH<sub>4</sub> surface coverage for  $f_{CH4} = 8\%$  favors growth of the hexagonal  $\beta$ -Mo<sub>2</sub>C over the cubic  $\delta$ -MoC<sub> $\nu$ </sub>. We speculate that continued growth beyond the thickness of our experiments will ultimately lead to a single dominant carbide phase or that C surface segregation will eventually cause a transition to a nanocrystalline/amorphous composite microstructure. If the CH<sub>4</sub> content in the processing gas is insufficient ( $f_{CH4} \le 6\%$ ) for  $\delta$ -MoC<sub> $\nu$ </sub> nucleation, the resulting layer exhibits a  $\beta$ -Mo<sub>2</sub>C (plus bcc Mo) phase. Conversely,  $f_{CH4} \ge 10\%$  is too large for β-Mo<sub>2</sub>C nucleation, yielding layers with a δ- $MoC_{\nu}$  (plus a-C) phase.

## IV. CONCLUSIONS

Molybdenum carbide thin films were deposited by reactive DC magnetron sputtering in an Ar-CH<sub>4</sub> gas mixture at 1200 °C onto Al<sub>2</sub>O<sub>3</sub>(0001) single crystal substrates with varying methane content  $f_{\text{CH4}} = 0$ -10%. The increase in  $f_{\text{CH4}}$  leads to a 3-fold reduction in the Mo sputtering rate and an increase in the voltage required to sustain a plasma. It also leads to a transition from bcc Mo to mixed-phase microstructures containing bcc Mo,  $\beta$ -Mo<sub>2</sub>C,  $\delta$ -MoC<sub>y</sub> and eventually nanocrystalline  $\delta$ -MoC<sub>y</sub> embedded in a-C. In particular  $f_{\text{CH4}} = 7$ -8% results a competitive growth mode between epitaxial  $\beta$ -Mo<sub>2</sub>C(0001) and  $\delta$ -MoC<sub>y</sub>(111) grains which nucleate on the substrate or grow epitaxially on nuclei of the competing phase. In addition, the film density decreases after the nucleation stage, suggesting that excess C forms amorphous clusters. The 111-oriented epitaxial  $\delta$ -MoC<sub>y</sub> has an in-plane epitaxial relationship with the substrate with [11 $\bar{2}$ ] $\delta$ -MoC || [11 $\bar{2}$ 0]<sub>Al2O3</sub>, while the 0001-oriented biaxial  $\beta$ -Mo<sub>2</sub>C exhibits a relatively large  $\pm$  25° variation in the in-plane orientation.

#### **ACKNOWLEDGEMENTS**

The authors acknowledge financial support by the National Science Foundation under Grant Nos. 1712752 and 1629230.

#### REFERENCES

- [1] E. Martínez, U. Wiklund, J. Esteve, F. Montalà, L.L. Carreras, Tribological performance of TiN supported molybdenum and tantalum carbide coatings in abrasion and sliding contact, Wear, 253 (2002) 1182-1187.
- [2] L.E. Toth, Transition metal carbides and nitrides, Academic Press, 1971.
- [3] L. Yang, C. Liu, M. Wen, X. Dai, Y. Zhang, X. Chen, K. Zhang, Small atoms as reinforced agent for both hardness and toughness of Group-VIB transition metal films, Journal of Alloys and Compounds, 735 (2018) 1105-1110.
- [4] S. Fritze, P. Malinovskis, L. Riekehr, L. von Fieandt, E. Lewin, U. Jansson, Hard and crack resistant carbon supersaturated refractory nanostructured multicomponent coatings, Scientific reports, 8 (2018) 1-8.
- [5] L. Yang, K. Zhang, Y. Zeng, X. Wang, S. Du, C. Tao, P. Ren, X. Cui, M. Wen, Boron doped bcc-W films: achieving excellent mechanical properties and tribological performance by regulating substrate bias voltage, Applied Surface Science, 423 (2017) 275-282.
- [6] L. Yang, K. Zhang, M. Wen, Z. Hou, C. Gong, X. Liu, C. Hu, X. Cui, W. Zheng, Highly hard yet toughened bcc-W coating by doping unexpectedly low B content, Scientific reports, 7 (2017) 1-8.
- [7] J. Garcia, V.C. Cipres, A. Blomqvist, B. Kaplan, Cemented carbide microstructures: a review, International Journal of Refractory Metals and Hard Materials, 80 (2019) 40-68.
- [8] H. Saito, A. Iwabuchi, T. Shimizu, Effects of Co content and WC grain size on wear of WC cemented carbide, Wear, 261 (2006) 126-132.
- [9] N. Nedfors, O. Tengstrand, E. Lewin, A. Furlan, P. Eklund, L. Hultman, U. Jansson, Structural, mechanical and electrical-contact properties of nanocrystalline-NbC/amorphous-C coatings deposited by magnetron sputtering, Surface and Coatings Technology, 206 (2011) 354-359.
- [10] K. Nygren, M. Samuelsson, A. Flink, H. Ljungcrantz, Å. Kassman Rudolphi, U. Jansson, Growth and characterization of chromium carbide films deposited by high rate reactive magnetron sputtering for electrical contact applications, Surface and Coatings Technology, 260 (2014) 326-334.
- [11] J.-L. Tsai, Q.-S. Luo, P.-R. Chen, Y.-H. Chen, MoC intermediate layer for FePt magnetic recording media, Journal of Applied Physics, 115 (2014).
- [12] Y. Zhong, X. Xia, F. Shi, J. Zhan, J. Tu, H.J. Fan, Transition Metal Carbides and Nitrides in Energy Storage and Conversion, Advanced Science, 3 (2016) 1500286.
- [13] W.-F. Chen, J.T. Muckerman, E. Fujita, Recent developments in transition metal carbides and nitrides as hydrogen evolution electrocatalysts, Chemical Communications, 49 (2013) 8896-8909.
- [14] Q. Gao, W. Zhang, Z. Shi, L. Yang, Y. Tang, Structural Design and Electronic Modulation of Transition-Metal-Carbide Electrocatalysts toward Efficient Hydrogen Evolution, Adv Mater, 31 (2019) e1802880.
- [15] U. Jansson, E. Lewin, Sputter deposition of transition-metal carbide films A critical review from a chemical perspective, Thin Solid Films, 536 (2013) 1-24.
- [16] B. Gao, X. Li, K. Ding, C. Huang, Q. Li, P. K. Chu, K. Huo, Recent progress in nanostructured transition metal nitrides for advanced electrochemical energy storage, Journal of Materials Chemistry A, 7 (2019) 14-37.

- [17] H. Vrubel, X. Hu, Molybdenum boride and carbide catalyze hydrogen evolution in both acidic and basic solutions, Angew Chem Int Ed Engl, 51 (2012) 12703-12706.
- [18] M. Miao, J. Pan, T. He, Y. Yan, B.Y. Xia, X. Wang, Molybdenum Carbide-Based Electrocatalysts for Hydrogen Evolution Reaction, Chemistry A European Journal, 23 (2017) 10947-10961.
- [19] A. Ruban, B. Hammer, P. Stoltze, H.L. Skriver, J.K. Nørskov, Surface electronic structure and reactivity of transition and noble metals, Journal of Molecular Catalysis A: Chemical, 115 (1997) 421-429.
- [20] V. Pallassana, M. Neurock, L.B. Hansen, B. Hammer, J.K. Nørskov, Theoretical analysis of hydrogen chemisorption on Pd (111), Re (0001) and Pd ML/Re (0001), Re ML/Pd (111) pseudomorphic overlayers, Physical Review B, 60 (1999) 6146.
- [21] H.B. Wu, B.Y. Xia, L. Yu, X.Y. Yu, X.W. Lou, Porous molybdenum carbide nano-octahedrons synthesized via confined carburization in metal-organic frameworks for efficient hydrogen production, Nat Commun, 6 (2015) 6512.
- [22] C. Tang, H. Zhang, K. Xu, Q. Zhang, J. Liu, C. He, L. Fan, T. Asefa, Unconventional molybdenum carbide phases with high electrocatalytic activity for hydrogen evolution reaction, Journal of Materials Chemistry A, 7 (2019) 18030-18038.
- [23] Z.W. Seh, K.D. Fredrickson, B. Anasori, J. Kibsgaard, A.L. Strickler, M.R. Lukatskaya, Y. Gogotsi, T.F. Jaramillo, A. Vojvodic, Two-Dimensional Molybdenum Carbide (MXene) as an Efficient Electrocatalyst for Hydrogen Evolution, ACS Energy Letters, 1 (2016) 589-594.
- [24] P. Xiao, X. Ge, H. Wang, Z. Liu, A. Fisher, X. Wang, Novel Molybdenum Carbide— Tungsten Carbide Composite Nanowires and Their Electrochemical Activation for Efficient and Stable Hydrogen Evolution, Advanced Functional Materials, 25 (2015) 1520-1526.
- [25] J.-S. Li, Y. Wang, C.-H. Liu, S.-L. Li, Y.-G. Wang, L.-Z. Dong, Z.-H. Dai, Y.-F. Li, Y.-Q. Lan, Coupled molybdenum carbide and reduced graphene oxide electrocatalysts for efficient hydrogen evolution, Nature communications, 7 (2016) 1-8.
- [26] Z. Cheng, Q. Fu, Q. Han, Y. Xiao, Y. Liang, Y. Zhao, L. Qu, A type of 1 nm molybdenum carbide confined within carbon nanomesh as highly efficient bifunctional electrocatalyst, Advanced Functional Materials, 28 (2018) 1705967.
- [27] Y. Liu, G. Yu, G.D. Li, Y. Sun, T. Asefa, W. Chen, X. Zou, Coupling Mo<sub>2</sub>C with nitrogen-rich nanocarbon leads to efficient hydrogen-evolution electrocatalytic sites, Angewandte Chemie, 127 (2015) 10902-10907.
- [28] S. Jing, L. Zhang, L. Luo, J. Lu, S. Yin, P.K. Shen, P. Tsiakaras, N-Doped Porous Molybdenum Carbide Nanobelts as Efficient Catalysts for Hydrogen Evolution Reaction, Applied Catalysis B: Environmental, 224 (2018) 533-540.
- [29] Y. Huang, J. Ge, J. Hu, J. Zhang, J. Hao, Y. Wei, Nitrogen-Doped Porous Molybdenum Carbide and Phosphide Hybrids on a Carbon Matrix as Highly Effective Electrocatalysts for the Hydrogen Evolution Reaction, Advanced Energy Materials, 8 (2018) 1701601.
- [30] R. Ge, J. Huo, M. Sun, M. Zhu, Y. Li, S. Chou, W. Li, Surface and Interface Engineering: Molybdenum Carbide-Based Nanomaterials for Electrochemical Energy Conversion, Small, (2019) e1903380.
- [31] Z. Zhao, F. Qin, S. Kasiraju, L. Xie, M.K. Alam, S. Chen, D. Wang, Z. Ren, Z. Wang, L.C. Grabow, Vertically aligned MoS<sub>2</sub>/Mo<sub>2</sub>C hybrid nanosheets grown on carbon paper for efficient electrocatalytic hydrogen evolution, ACS Catalysis, 7 (2017) 7312-7318.

- [32] J. Jeon, Y. Park, S. Choi, J. Lee, S.S. Lim, B.H. Lee, Y.J. Song, J.H. Cho, Y.H. Jang, S. Lee, Epitaxial synthesis of molybdenum carbide and formation of a Mo<sub>2</sub>C/MoS<sub>2</sub> hybrid structure via chemical conversion of molybdenum disulfide, ACS nano, 12 (2018) 338-346.
- [33] B.D. Ozsdolay, C.P. Mulligan, M. Guerette, L. Huang, D. Gall, Epitaxial growth and properties of cubic WN on MgO(001), MgO(111), and Al<sub>2</sub>O<sub>3</sub>(0001), Thin Solid Films, 590 (2015) 276-283.
- [34] D. Gall, I. Petrov, N. Hellgren, L. Hultman, J.E. Sundgren, J.E. Greene, Growth of polyand single-crystal ScN on MgO(001): Role of low-energy N<sub>2</sub><sup>+</sup> irradiation in determining texture, microstructure evolution, and mechanical properties, Journal of Applied Physics, 84 (1998) 6034-6041.
- [35] R. Deng, S.R. Evans, D. Gall, Bandgap in Al<sub>1-x</sub>Sc<sub>x</sub>N, Applied Physics Letters, 102 (2013) 112103.
- [36] C.-S. Shin, D. Gall, N. Hellgren, J. Patscheider, I. Petrov, J.E. Greene, Vacancy hardening in single-crystal  $TiN_x(001)$  layers, Journal of Applied Physics, 93 (2003) 6025-6028.
- [37] J.S. Chawla, X.Y. Zhang, D. Gall, Effective electron mean free path in TiN(001), Journal of Applied Physics, 113 (2013) 063704.
- [38] B.D. Ozsdolay, K. Balasubramanian, D. Gall, Cation and anion vacancies in cubic molybdenum nitride, Journal of Alloys and Compounds, 705 (2017) 631-637.
- [39] M.E. McGahay, D. Gall, Conductive surface oxide on CrN(001) layers, Applied Physics Letters, 114 (2019) 131602.
- [40] B. Wang, D. Gall, Fully strained epitaxial Ti<sub>1-x</sub>Mg<sub>x</sub>N(001) layers, Thin Solid Films, (2019).
- [41] K. Zhang, K. Balasubramanian, B.D. Ozsdolay, C.P. Mulligan, S.V. Khare, W.T. Zheng, D. Gall, Growth and mechanical properties of epitaxial NbN(001) films on MgO(001), Surface and Coatings Technology, 288 (2016) 105-114.
- [42] H.-S. Seo, T.-Y. Lee, J.G. Wen, I. Petrov, J.E. Greene, D. Gall, Growth and physical properties of epitaxial HfN layers on MgO(001), Journal of Applied Physics, 96 (2004) 878-884.
- [43] D. Gall, C.-S. Shin, T. Spila, M. Odén, M.J.H. Senna, J.E. Greene, I. Petrov, Growth of single-crystal CrN on MgO(001): Effects of low-energy ion-irradiation on surface morphological evolution and physical properties, Journal of Applied Physics, 91 (2002) 3589-3597.
- [44] C.-S. Shin, Y.-W. Kim, D. Gall, J. Greene, I. Petrov, Phase composition and microstructure of polycrystalline and epitaxial  $TaN_x$  layers grown on oxidized Si(001) and MgO(001) by reactive magnetron sputter deposition, Thin Solid Films, 402 (2002) 172-182.
- [45] X.Y. Zhang, J.S. Chawla, B.M. Howe, D. Gall, Variable-range hopping conduction in epitaxial CrN(001), Physical Review B, 83 (2011) 165205.
- [46] A. B. Mei, M. Tuteja, D. G. Sangiovanni, R. T. Haasch, A. Rockett, L. Hultman, I. Petrov, J. E. Greene, Growth, nanostructure, and optical properties of epitaxial  $VN_x/MgO(001)$  (0.80  $\leq$
- $x \le 1.00$ ) layers deposited by reactive magnetron sputtering, Journal of Materials Chemistry C, 4 (2016) 7924-7938.
- [47] M. Braic, N.C. Zoita, M. Danila, C.E.A. Grigorescu, C. Logofatu, Hetero-epitaxial growth of TiC films on MgO(001) at 100°C by DC reactive magnetron sputtering, Thin Solid Films, 589 (2015) 590-596.
- [48] J. Carroll, R. Krchnavek, C. Lunk, T. Scabarozi, S. Lofland, J. Hettinger, An investigation of the properties of epitaxial chromium-substituted vanadium carbide thin films, Vacuum, 109 (2014) 212-215.

- [49] K. Zhang, K. Balasubramanian, B. Ozsdolay, C. Mulligan, S. Khare, W. Zheng, D. Gall, Epitaxial NbC $_x$ N $_{1-x}$  (001) layers: Growth, mechanical properties, and electrical resistivity, Surface and Coatings Technology, 277 (2015) 136-143.
- [50] H. Zaid, A. Aleman, K. Tanaka, C. Li, P. Berger, T. Back, J. Fankhauser, M.S. Goorsky, S. Kodambaka, Influence of ultra-low ethylene partial pressure on microstructural and compositional evolution of sputter-deposited Zr-C thin films, Surface and Coatings Technology, 398 (2020).
- [51] S. Kacim, L. Binst, F. Reniers, F. Bouillon, Composition and structure of reactively sputter-deposited molybdenum-carbon films, Thin Solid Films, 287 (1996) 25-31.
- [52] U. Jansson, H. Högberg, J.-P. Palmqvist, L. Norin, J.O. Malm, L. Hultman, J. Birch, Low temperature epitaxial growth of metal carbides using fullerenes, Surface and Coatings Technology, 142-144 (2001) 817-822.
- [53] P. Fang, B. Wang, C. Mulligan, T. Murray, S. Khare, D. Gall, Epitaxial growth of cubic WC<sub>v</sub> (001) on MgO (001), Journal of Alloys and Compounds, 860 (2021) 158403.
- [54] J. Lu, H. Hugosson, O. Eriksson, L. Nordström, U. Jansson, Chemical vapour deposition of molybdenum carbides: aspects of phase stability, Thin Solid Films, 370 (2000) 203-212.
- [55] M. Trgala, M. Žemlička, P. Neilinger, M. Rehák, M. Leporis, Š. Gaži, J. Greguš, T. Plecenik, T. Roch, E. Dobročka, M. Grajcar, Superconducting MoC thin films with enhanced sheet resistance, Applied Surface Science, 312 (2014) 216-219.
- [56] H.W. Hugosson, O. Eriksson, L. Nordström, U. Jansson, L. Fast, A. Delin, J.M. Wills, B. Johansson, Theory of phase stabilities and bonding mechanisms in stoichiometric and substoichiometric molybdenum carbide, Journal of Applied Physics, 86 (1999) 3758-3767.
- [57] G.L. Hart, B.M. Klein, Phonon and elastic instabilities in MoC and MoN, Physical Review B, 61 (2000) 3151.
- [58] C. Tripathi, M. Kumar, D. Kumar, Atom beam sputtered Mo<sub>2</sub>C films as a diffusion barrier for copper metallization, Applied Surface Science, 255 (2009) 3518-3522.
- [59] T. Kado, Epitaxial molybdenum oxycarbide thin films synthesized by inductively coupled radio-frequency plasma assisted magnetron sputtering, Thin Solid Films, 515 (2006) 2481-2484.
- [60] P. Malinovskis, J. Palisaitis, P.O.Å. Persson, U. Jansson, E. Lewin, Synthesis and characterisation of Mo-B-C thin films deposited by non-reactive DC magnetron sputtering, Surface and Coatings Technology, 309 (2017) 506-515.
- [61] D.D. Kumar, N. Kumar, K. Panda, A.M. Kamalan Kirubaharan, P. Kuppusami, Tribochemistry of contact interfaces of nanocrystalline molybdenum carbide films, Applied Surface Science, 447 (2018) 677-686.
- [62] R. Liu, G. Luo, Y. Li, J. Zhang, Q. Shen, L. Zhang, Microstructure and thermal properties of diamond/copper composites with Mo2C in-situ nano-coating, Surface and Coatings Technology, 360 (2019) 376-381.
- [63] J. Qian, S. Li, J. Pu, Z. Cai, H. Wang, Q. Cai, P. Ju, Effect of heat treatment on structure and properties of molybdenum nitride and molybdenum carbonitride films prepared by magnetron sputtering, Surface and Coatings Technology, 374 (2019) 725-735.
- [64] A. Bertuch, B.D. Keller, N. Ferralis, J.C. Grossman, G. Sundaram, Plasma enhanced atomic layer deposition of molybdenum carbide and nitride with bis(tert-butylimido)bis(dimethylamido) molybdenum, Journal of Vacuum Science & Technology A: Vacuum, Surfaces, and Films, 35 (2017).

- [65] Z. Zhang, F. Zhang, H. Wang, C. Ho Chan, W. Lu, J.-y. Dai, Substrate orientation-induced epitaxial growth of face centered cubic Mo<sub>2</sub>C superconductive thin film, J. Mater. Chem. C, 5 (2017) 10822-10827.
- [66] E. Milosevic, S. Kerdsongpanya, A. Zangiabadi, K. Barmak, K.R. Coffey, D. Gall, Resistivity size effect in epitaxial Ru(0001) layers, Journal of Applied Physics, 124 (2018) 165105.
- [67] L.G. Parratt, Surface studies of solids by total reflection of X-rays, Physical review, 95 (1954) 359.
- [68] M. Mayer, Improved physics in SIMNRA 7, Nuclear Instruments and Methods in Physics Research Section B: Beam Interactions with Materials and Atoms, 332 (2014) 176-180.
- [69] E.V. Bogatyreva, A.G. Ermilov, Evaluating the Energy Content of Nonequilibrium Tungsten and Molybdenum Carbide Structures, Powder Metallurgy and Metal Ceramics, 53 (2014) 431-440.
- [70] A. Zelikman, Molybdenum, IZDATELSTVO METALLURGIYA, MOSCOW. 1970, 440 P, (1970).
- [71] R.H. Willens, E. Buehler, The Superconductivity of the Monocarbides of Tungsten and Molybdenum, Applied Physics Letters, 7 (1965) 25-26.
- [72] J.R.d.S. Politi, F. Viñes, J.A. Rodriguez, F. Illas, Atomic and electronic structure of molybdenum carbide phases: bulk and low Miller-index surfaces, Physical Chemistry Chemical Physics, 15 (2013) 12617.
- [73] A. Vojvodic, Steam Reforming on Transition-Metal Carbides from Density-Functional Theory, Catalysis Letters, 142 (2012) 728-735.
- [74] W.D. Sproul, D.J. Christie, D.C. Carter, Control of reactive sputtering processes, Thin Solid Films, 491 (2005) 1-17.
- [75] C.-S. Shin, Y.-W. Kim, D. Gall, J.E. Greene, I. Petrov, Phase composition and microstructure of polycrystalline and epitaxial TaNx layers grown on oxidized Si(001) and MgO(001) by reactive magnetron sputter deposition, Thin Solid Films, 402 (2002) 172-182.
- [76] O. Fouad, A.K. Rumaiz, S.I. Shah, Reactive sputtering of titanium in Ar/CH<sub>4</sub> gas mixture: Target poisoning and film characteristics, Thin Solid Films, 517 (2009) 5689-5694.
- [77] V. Krajnik, A. Lisenko, E. Zhurakovskij, V. Ivashchenko, Influence of nonmetallic and metallic vacancies on the stability of cubic molybdenum carbide, Doklady Akademii Nauk SSSR, 307 (1989) 1365-1369.
- [78] W. Sun, H. Ehteshami, P.A. Korzhavyi, Structure and energy of point defects in TiC: An ab initio study, Physical Review B, 91 (2015) 134111.
- [79] G. Katz, The epitaxy of copper on sapphire, Applied Physics Letters, 12 (1968) 161-163.
- [80] A. Jog, T. Zhou, D. Gall, Resistivity Size Effect in Epitaxial Rh (001) and Rh (111) Layers, IEEE Transactions on Electron Devices, 68 (2020) 257-263.
- [81] K. Balasubramanian, S.V. Khare, D. Gall, Valence electron concentration as an indicator for mechanical properties in rocksalt structure nitrides, carbides and carbonitrides, Acta Materialia, 152 (2018) 175-185.

# Figures:

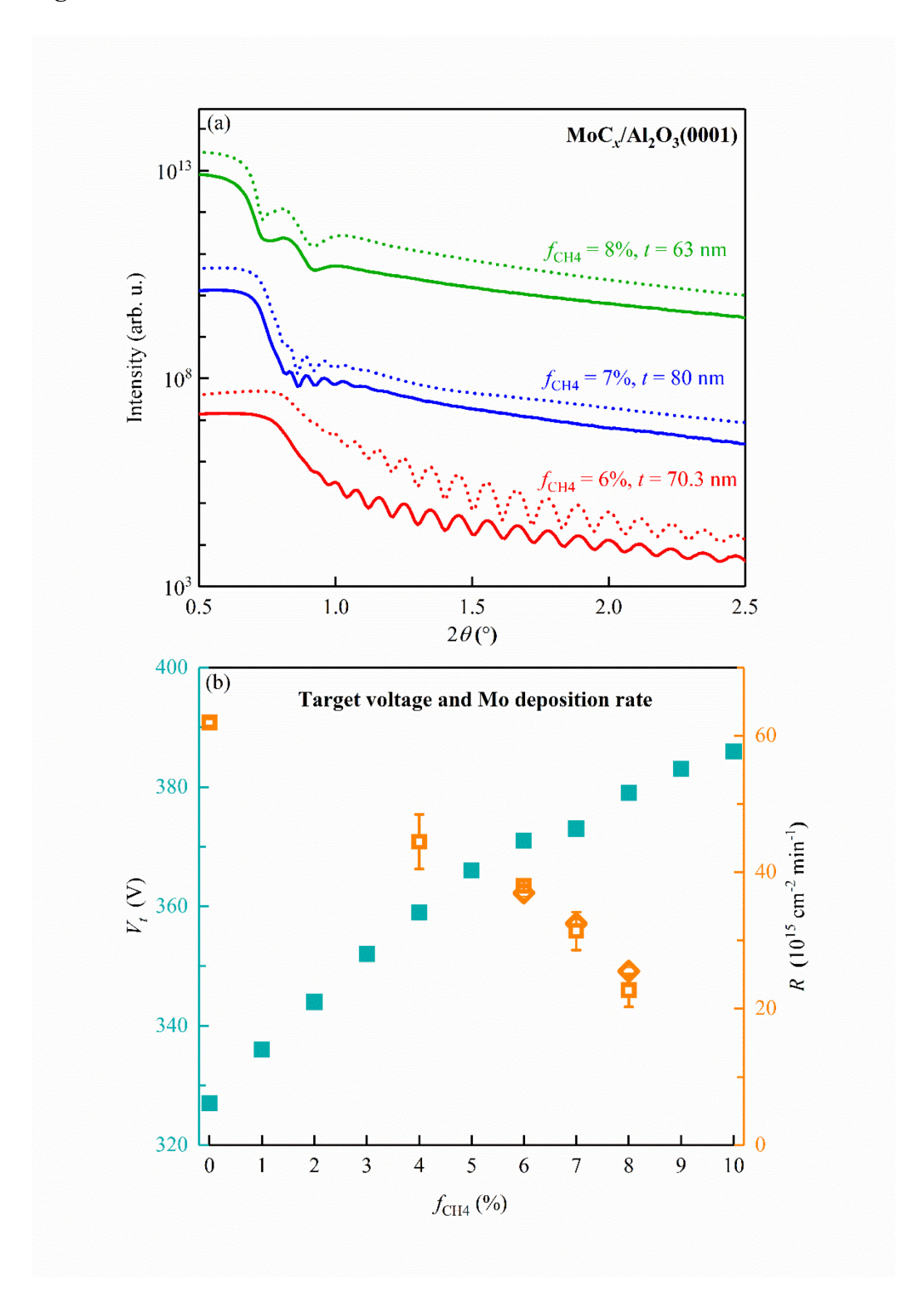


**Fig. 1.** (a) Measured X-ray reflectivity from three  $MoC_x$  layers deposited with a methane gas fraction  $f_{CH4} = 6\%$ , 7% and 8%. The dotted lines are the result from curve fitting. (b) The discharge voltage  $V_t$  during deposition and the Mo deposition rate R vs  $f_{CH4}$ .

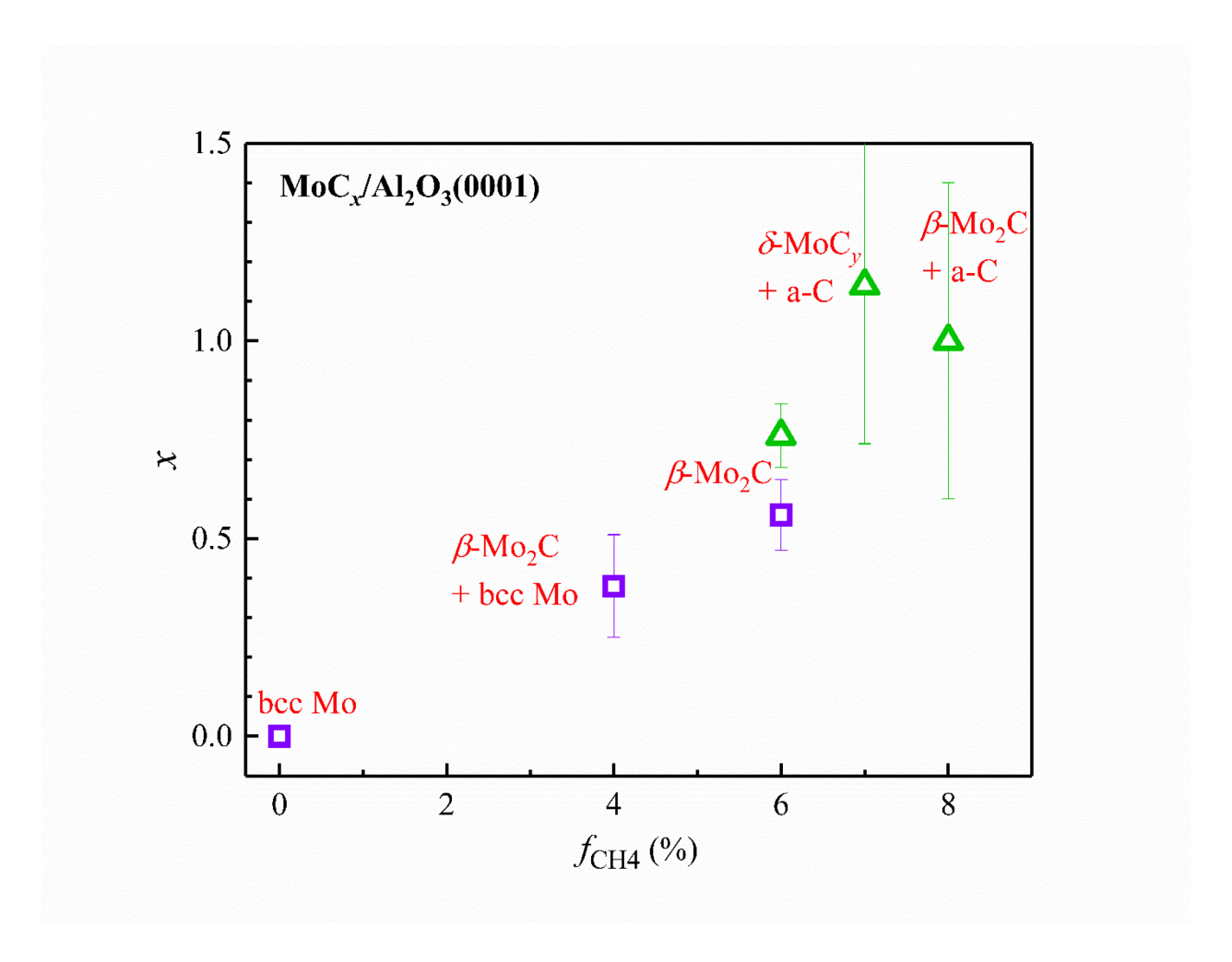


**Fig. 2.** The total C-to-Mo ratio x in MoC<sub>x</sub> layers vs methane gas fraction  $f_{CH4}$ , as determined from XRR analyses (purple squares) and a combination of RBS and XRR measurements (green triangles).

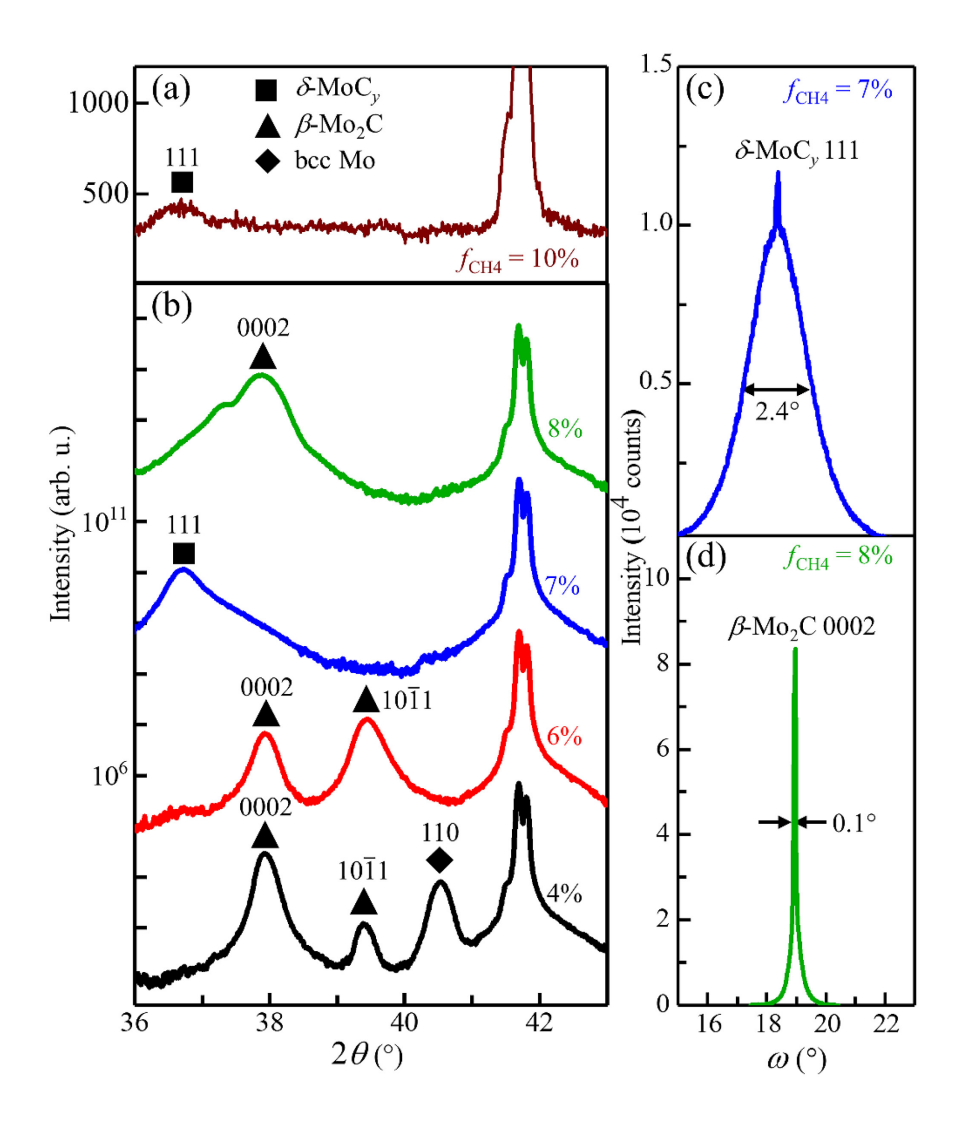


**Fig. 3.** X-ray diffraction  $\theta$ -2  $\theta$  patterns from MoC<sub>x</sub>/Al<sub>2</sub>O<sub>3</sub>(0001) layers obtained with (a) a divergent beam geometry for  $f_{\text{CH4}} = 10\%$  and (b) a parallel beam geometry for  $f_{\text{CH4}} = 4$ -8%. ω-rocking curves of the (c) δ-MoC<sub>y</sub> 111 and (d) β-Mo<sub>2</sub>C 0002 reflections from layers deposited with  $f_{\text{CH4}} = 7\%$  and 8%, respectively.

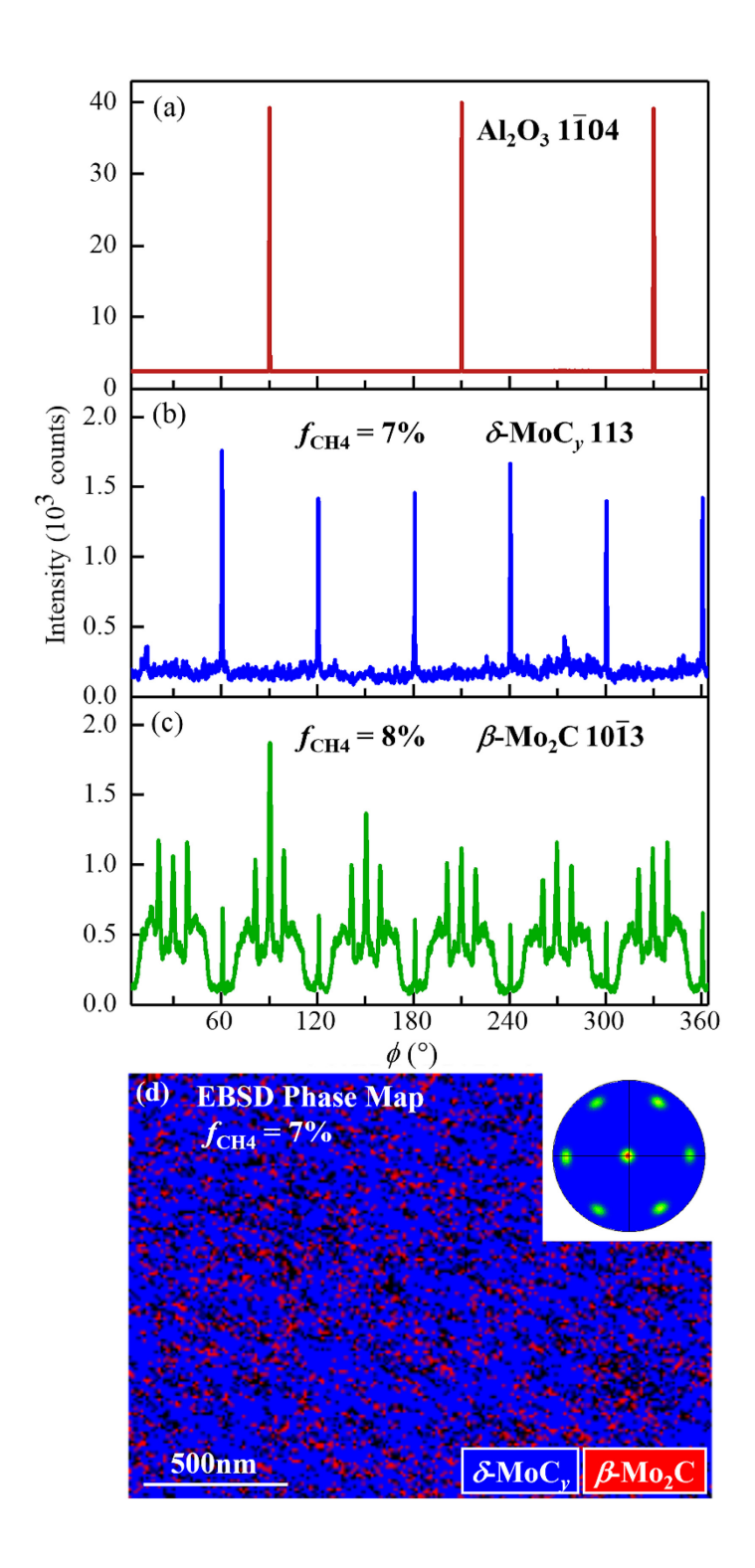


**Fig. 4.** X-ray diffraction  $\phi$ -scans for (a) Al<sub>2</sub>O<sub>3</sub> 1 $\overline{1}$ 04, (b)  $\delta$ -MoC<sub>y</sub> 113, and (c)  $\beta$ -Mo<sub>2</sub>C 10 $\overline{1}$ 3 reflections from MoC<sub>x</sub>/Al<sub>2</sub>O<sub>3</sub>(0001) layers deposited with  $f_{CH4} = 7$  or 8%, as labeled. (d) Electron backscatter diffraction phase map from a  $f_{CH4} = 7$ % layer, including a  $\delta$ -MoC<sub>y</sub> {111} pole figure in the inset.

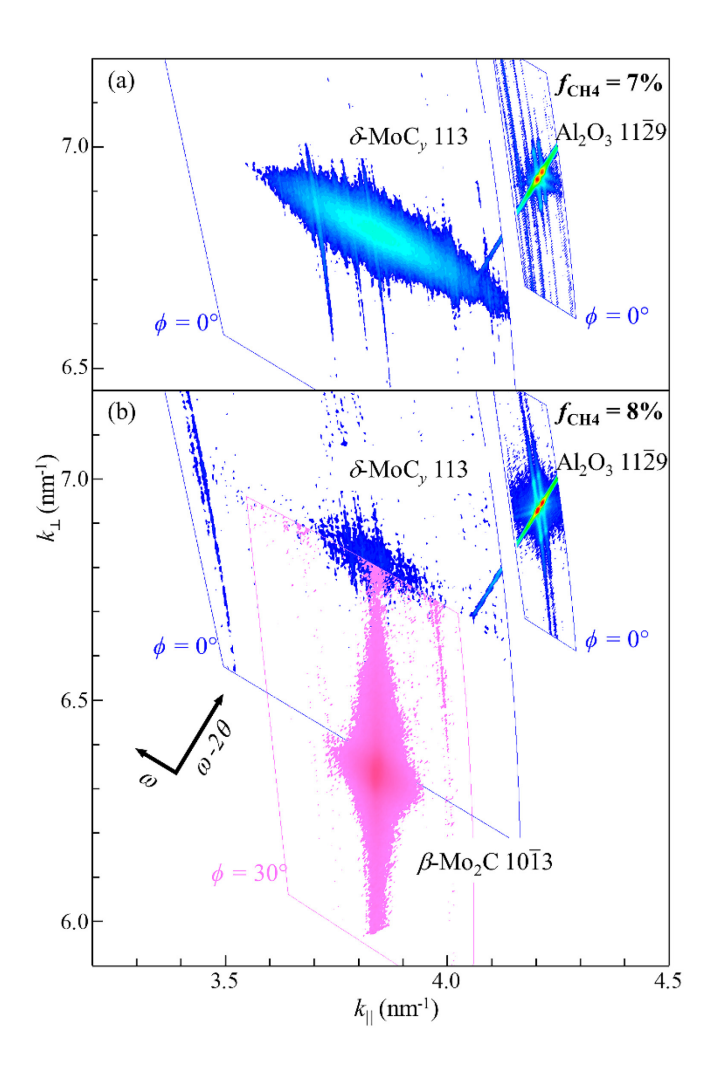


**Fig. 5.** XRD reciprocal space maps from  $MoC_x/Al_2O_3(0001)$  layers deposited at (a)  $f_{CH4} = 7\%$  and (b)  $f_{CH4} = 8\%$ , taken at  $\phi = 0^\circ$  for  $\delta$ -MoC<sub>y</sub> 113 and Al<sub>2</sub>O<sub>3</sub> 11 $\overline{2}$ 9 reflections (blue-to-red contours) and at  $\phi = 30^\circ$  for  $\beta$ -Mo<sub>2</sub>C  $10\overline{1}$ 3 (pink-to-red contours).